Electrochemistry Communications 114 (2020) 106716

Contents lists available at ScienceDirect

Electrochemistry Communications

journal homepage: www.elsevier.com/locate/elecom

Synergistic Cu/CeO_2 carbon nanofiber catalysts for efficient CO_2 electroreduction

Xin Zong[a,1], Jie Zhang[b,c,1], Jinqiu Zhang[a], Wen Luo[b,c,*], Andreas Züttel[b,c], Yueping Xiong[a,*]

[a] MIIT Key Laboratory of Critical Materials Technology for New Energy Conversion and Storage, School of Chemistry and Chemical Engineering, Harbin Institute of Technology, Harbin 150001, PR China

[b] Laboratory of Materials for Renewable Energy (LMER), Institute of Chemical Sciences and Engineering (ISIC), Basic Science Faculty (SB), École Polytechnique Fédérale de Lausanne (EPFL) Valais/Wallis, Energypolis, Rue de l'Industrie 17, CH-1951 Sion, Switzerland

[c] Empa Materials Science & Technology, CH-8600 Dübendorf, Switzerland

ARTICLE INFO

Keywords:
Copper
Ceria
Electrospinning
CO_2 electroreduction
Flow cell

ABSTRACT

The electrochemical reduction of carbon dioxide (CO_2RR) has attracted enormous interest because of the energy crisis and climate change; however, more efficient catalysts are required for practical applications. Herein, we present electrospinning as a facile strategy to synthesize a three-dimensional network of carbon nanofibers embedded with Cu and CeO_x nanoparticles (Cu/CeO_x@CNFs) as a CO_2RR catalyst. The Cu–CeO_x interface produced using this method offers synergistic geometric and electronic effects which optimize the adsorption strength of reaction intermediates for the electroreduction of CO_2 to CO. In a flow cell configuration, a current density of 100 mA cm^{-2} and a CO faradaic efficiency of 59.2% can be obtained at −0.60 V vs. RHE.

1. Introduction

With the massive use of fossil fuels, the concentration of carbon dioxide in the atmosphere now exceeds 415 ppm, a level which last occurred 3 million years ago [1]. Electrochemical reduction of carbon dioxide (CO_2) using renewable energy is a promising method of reducing the CO_2 in the atmosphere and developing a carbon–neutral cycle [2]. Due to the thermodynamic stability of CO_2 [3], the redox potential of CO_2/CO_2 to form energetic CO_2^- radicals is as negative as −1.9 V (vs. RHE) [4]. As a result, the effective activation of C═O constrains CO_2 electroreduction [5]. It is therefore important to design efficient catalysts for CO_2 electroreduction. However, there are still several bottlenecks that limit catalyst efficiency, including competition between the CO_2 reduction and hydrogen evolution reactions, low current density and poor product selectivity. Among transition metals, Cu-based catalysts have attracted widespread interest because of their outstanding ability to reduce CO_2 not only into two-electron transfer products (e.g., carbon monoxide [6–8] and formic acid [9]) but also into multi-electron transfer products (e.g., methane [10], methanol [11], ethylene [12,13] and ethanol [14]). Many studies have been dedicated to improving the performance of Cu-based catalysts by controlling their size, morphology, structure and composition [15,16]. However, a major challenge for Cu-based catalysts is the weak adsorption of CO_2 on the catalyst surface [17]. Thus, it is crucial to design catalysts which are capable of converting CO_2 into energetic molecules by capturing CO_2 and activating C═O.

Recently, some researchers have reported that synergistic effects can enhance CO_2 electroreduction by promoting CO_2 adsorption and activation. For example, the Au–CeO_2 interface enhances the conversion of CO_2 to CO by increasing the binding strength of *COOH and easing CO_2 activation [18]. In addition, the ideal interface between Ti and Au can maximize the electronic effect, which plays an important role in bonding with both CO and COOH adsorbates [19]. Nonetheless, a facile strategy to produce an efficient catalyst with a Cu–oxide interface is still required to scale up for real-world applications.

Herein, a series of copper/ceria–carbon nanofiber (Cu/CeO_x@CNFs) catalysts were synthesized using the electrospinning method. This method allows the in situ growth of Cu–CeO_x on a carbon nanofiber support, which enables the generation of a large metal–metal oxide interface. The high surface area of the one-dimensional nanofiber structure along with the highly distributed Cu and CeO_x sites are found to enhance the catalytic performance of CO_2RR. Enhanced CO selectivity has been achieved at a low overpotential with a high current density on a sample with an optimized Ce to Cu ratio.

* Corresponding author at: MIIT Key Laboratory of Critical Materials Technology for New Energy Conversion and Storage, School of Chemistry and Chemical Engineering, Harbin Institute of Technology, Harbin 150001, PR China (Y. Xiong).

E-mail addresses: wen.luo@epfl.ch (W. Luo), ypxiong@hit.edu.cn (Y. Xiong).

[1] Both authors contributed equally to this work.

https://doi.org/10.1016/j.elecom.2020.106716
Received 25 February 2020; Received in revised form 14 March 2020; Accepted 20 March 2020
Available online 22 March 2020

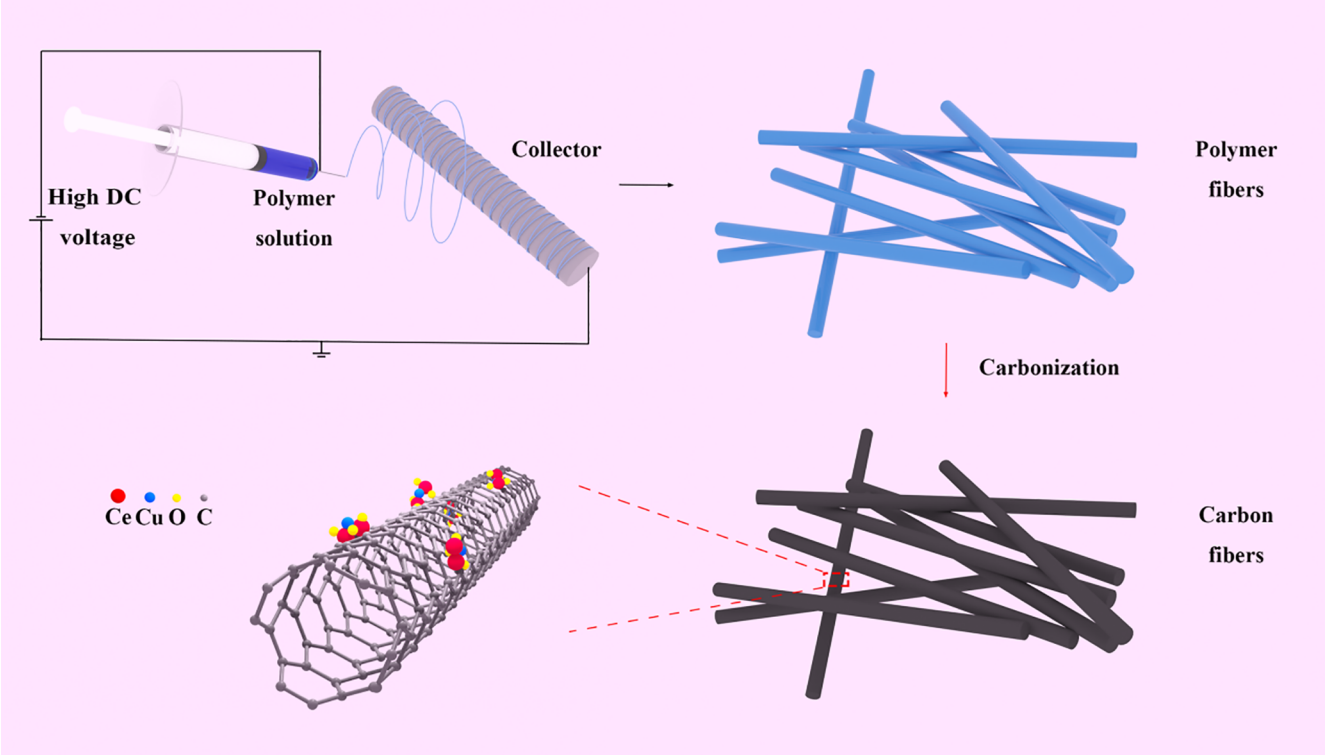

Fig. 1. Schematic of the synthesis of the Cu/CeO_x@CNFs catalysts.

2. Materials and methods

2.1. Materials

Sodium hydroxide (NaOH, 98%), potassium bicarbonate ($KHCO_3$, 99.7%), copper nitrate trihydrate ($Cu(NO_3)_2{\cdot}3H_2O$, 99%), and cerium nitrate hexahydrate ($Ce(NO_3)_3{\cdot}6H_2O$, 99.5%) were purchased from Aladdin. Nafion 117 solution (5 wt%) was purchased from Sigma-Aldrich. Polyvinylpyrrolidone (PVP, K90), *N*,*N*-dimethylformamide (DMF, 99%) and ethanol were purchased from Sinopharm Chemical Reagent Co., Ltd. Carbon paper was purchased from Toray Industries, Inc. Deionized water was produced using a Millipore system.

2.2. Synthesis of Cu/CeO_x@CNFs

Firstly, 1.5 g of $Cu(NO_3)_2{\cdot}3H_2O$ and $Ce(NO_3)_3{\cdot}6H_2O$ were added to 30 mL *N*,*N*-dimethylformamide (DMF) at molar ratios of 1:0.5, 1:1.5, or 1:2, and magnetically stirred at room temperature for two hours to obtain a homogeneous solution. Then 3.8 g polyvinylpyrrolidone (PVP) was added to the solution, and magnetically stirred for 10 h until the PVP was completely dissolved. The precursor solution was then removed into a syringe with a steel needle linked to a high-voltage power supply. We utilized high DC voltage at 30 kV to push the precursor solution spray into the nanofibers and a nickel net acted as a collector to receive polymer fiber from the parallel needles. Finally, the nanofibers were carbonized at 800 °C for 2 h at a heating rate of 5 °C·min^{-1} under N_2 atmosphere. We thus prepared a novel 3D carbon nanofiber network embedded with Cu and CeO_2 nanoparticles, and the different Cu/CeO_x@CNFs samples will be referred to as Cu/CeO_x@CNFs-n (where n represents the molar ratio of Ce/Cu, n = 0.5, 1.5, 2).

2.3. Preparation of gas diffusion layer

Catalyst inks were prepared by thoroughly mixing catalyst powder (4 mg) in ethanol (975 μL) with Nafion solution (25 μL). Working electrodes were prepared by drop-casting 0.65 mg cm^{-2} of the catalyst inks onto 1.0 cm^{-2} carbon paper, followed by drying at 70 °C.

2.4. Characterization

Scanning electron microscopy (SEM) images were obtained using a ZEISS system (SUPRA55010102) to investigate the morphology of the synthesized nanofibers. Synchrotron radiation X-ray diffraction (XRD) was carried out at the Shanghai Synchrotron Radiation Facility (SSRF) at 18 kV with a light source with λ = 0.6887 Å to determine the character of samples (Beamline BL14B1; detailed information about Beamline BL14B1 can be found in ref. [20]). Transmission electron microscopy (TEM, Tecnai G2 F30) and energy dispersive X-ray analysis (EDX) were performed on a FEI Tecnai F30. X-ray photoelectron spectroscopy (XPS, ESCALAB 250Xi, ThermoFisher) was used to analyze the composition and valency of the elements. Electron paramagnetic resonance studies (EPR, A200-9.5/12010602, Bruker) were performed to demonstrate the existence of oxygen vacancies.

2.5. Electrochemical measurements

The electrochemical tests were operated in a flow-cell reactor (**Fig. S1**) [21]. A piece of Ni film and a Ag/AgCl (3 M KCl) electrode were applied as the counter electrode and reference electrode, respectively. An anion exchange membrane (FAA-3-50) was used to separate the working electrode and counter electrode. The geometric surface area of both electrodes was 0.5 cm^2. Each compartment of the cell was filled with 1 M KOH aqueous solution. During the electrolysis process, CO_2 was constantly injected into the cell at a flow rate of 145 sccm and the cathodic electrolyte was injected at a flow rate of 0.4 mL min^{-1}.

The gas-phase products were detected by gas chromatography (GC, SRI instrument 8610C) with a thermal conductivity detector (TCD) and a flame ionization detector (FID). The liquid-phase products were collected and detected by high-performance liquid chromatography (HPLC, Thermo Scientific, Diones UltiMate 3000 Standard System).

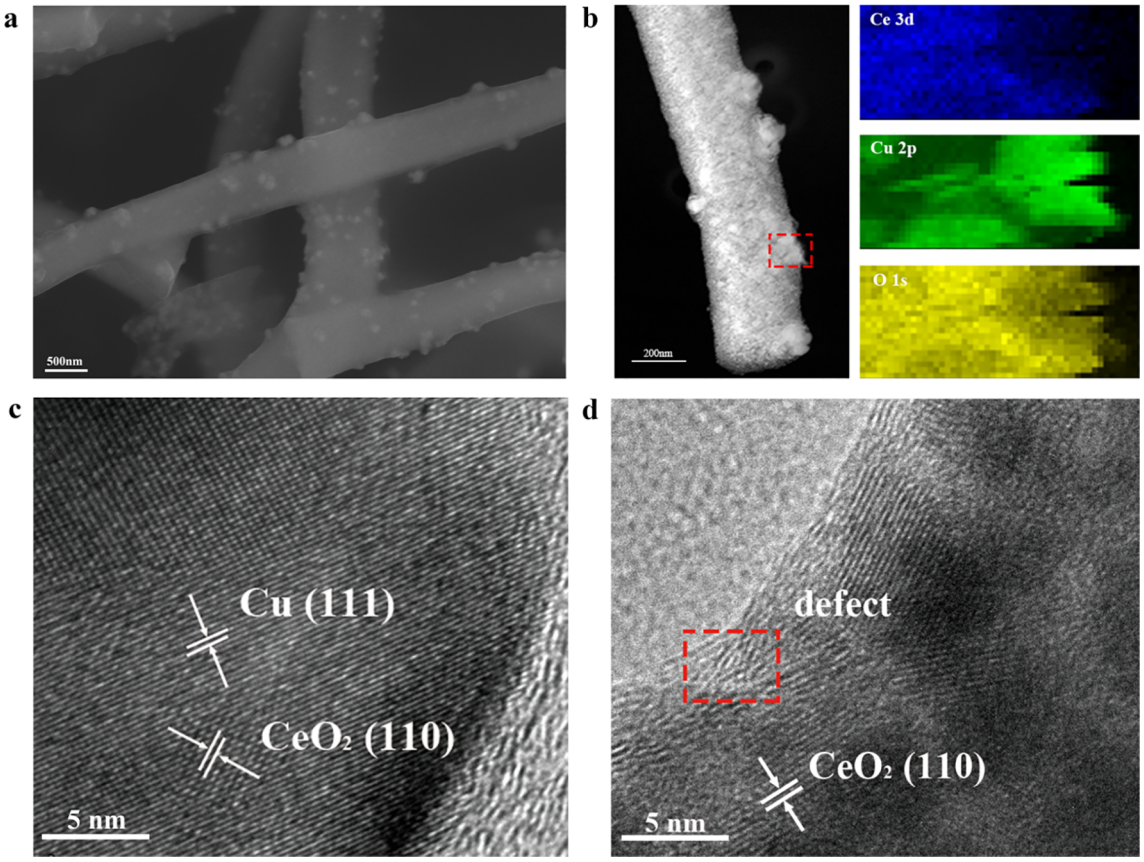

Fig. 2. (a) SEM image of Cu/CeO_x@CNFs-2; (b) HAADF-STEM image and EDX elemental maps of Cu/CeO_x@CNFs-2; (c) and (d) HRTEM images of Cu/CeO_x@CNFs-2.

3. Results and discussion

3.1. Synthesis and characterization of Cu/CeO_x-CNFs catalysts

The synthesis of Cu/CeO_x@CNFs is summarised schematically in Fig. 1. Firstly, a precursor solution with a given ratio of Cu^{2+} and Ce^{3+} was prepared by dissolving $Cu(NO_3)_2{\cdot}3H_2O$ and $Ce(NO_3)_3{\cdot}6H_2O$ in *N,N*-dimethylformamide (DMF). The ratio of Cu^{2+} and Ce^{3+} was controlled in order to optimize the surface content and interface sites of Cu and CeO_x. The precursor was then drawn into polymer fibers using a high voltage power source and Cu^{2+} and Ce^{3+} ions were dispersed on the polymer fibers. Finally, the polymer fibers were carbonized under nitrogen to form Cu/CeO_x nanoparticles embedded in the carbon nanofibers.

From the SEM image of the Cu/CeO_x@CNFs-2 sample (Fig. 2), we can see that the average diameter of the carbon fiber is about 400 nm and that the Cu–CeO_x nanoparticles are randomly distributed on the carbon fibers (SEM images of other Cu/CeO_x@CNFs-n samples are shown in **Fig. S2**). In addition, the carbon nanofibers stack on each other to form a 3D network with abundant pores, which enhances the electronic conductivity and gas diffusion efficiency. N_2 adsorption-desorption isotherms were used to characterize the specific surface area and pore structure of the fabricated samples. The N_2 adsorption-desorption curve of Cu/CeO_x@CNFs-2 (**Fig. S3**) shows an isotherm with type-IV properties, suggesting that Cu/CeO_x@CNFs-2 has a mesoporous structure [22]. A high specific surface area of 169.95 $m^2\ g^{-1}$ was obtained for Cu/CeO_x@CNFs-2, which is much larger than the specific surface area of 30.57 $m^2\ g^{-1}$ obtained for Cu@CNFs. This is because the addition of Ce tends to promote the formation of well-dispersed carbon fibers, compared to the carbon agglomerates produced when only Cu is added. Additionally, the pore size distribution for Cu/CeO_x@CNFs-2 is around 4.28 nm, much larger than the size of CO_2 molecules, and thus would facilitate gas transmission.

The detailed morphology and crystal structure of Cu/CeO_x@CNFs-2 catalyst were studied by TEM (Fig. 2 **and Fig. S4**). The energy dispersive X-ray (EDX) element maps of Cu/CeO_x@CNFs-2 (Fig. 2**b**) show that Cu and Ce species are highly mixed, demonstrating the homogeneous distribution of Cu and Ce. In the high-resolution TEM (HRTEM, Fig. 2**c**) image, the lattice fringes of 0.312 nm and 0.208 nm can be assigned to the (1 1 0) plane of CeO_2 and (1 1 1) plane of Cu, respectively, indicating that Cu did not replace Ce in CeO_2. Therefore, it is more likely that Cu and CeO_2 form small crystals (several nanometers) in close contact, which generate abundant interfaces between them. In addition, the HRTEM image of the disordered interface (square in Fig. 2**d**) indicates the existence of defects, which have been shown to be suitable as adsorption and activation sites for CO_2RR [23].

To clarify the bulk crystal structure of the catalysts, synchrotron radiation XRD was carried out and the resulting patterns are shown in Fig. 3. Because synchrotron radiation has high intensity, high collimation and a wide range of wavelengths, it can provide a more accurate analysis of the phase structure of the catalyst. For all the samples, the peak at 12.65° can be assigned to the (1 1 0) plane of CeO_2 while the peaks at 19.004° and 21.978° are ascribed to the (1 1 1) and (2 0 0) planes of Cu, respectively. No peak shift was observed on varying the Ce content, which again confirms our TEM results that Cu did not form mixed oxides with CeO_2 but rather produced separated crystalline species. Interestingly, most of the Cu in the catalysts is in the metallic state while Ce is in an oxide state, indicating that the high temperature and inert environment is sufficient to decompose the Cu^{2+} precursor into metallic Cu but cannot do the same for Ce^{3+}. In addition, low intensity peaks characteristic of Cu_2O (Fig. 3) are found for the sample with the highest Cu:Ce ratio (1:0.5 for Cu/CeO_x@CNFs-0.5), but not for the other samples, probably due to the low content and low crystallinity of Cu_2O in these cases.

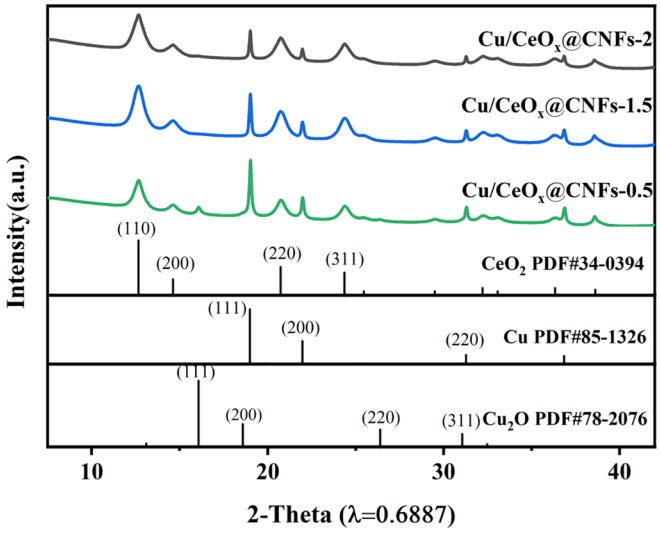

Fig. 3. Synchrotron radiation XRD patterns of Cu/CeO_x@CNFs-0.5, Cu/CeO_x@CNFs-1.5, and Cu/CeO_x@CNFs-2.

3.2. Catalytic activity of Cu/CeO_x@CNFs for electrochemical reduction of CO_2

The CO_2RR performance was measured in a flow-cell and 1.0 M KOH was used as the electrolyte in order to suppress H_2 evolution [21]. An anion exchange membrane was used to separate the catholyte and anolyte chambers. Gas-phase products were detected by GC and liquid-phase products were analyzed by HPLC. The product distribution in the current range 50–300 mA cm^{-2} is shown in Fig. 4 for the various Cu/CeO_x@CNFs-n samples and the Cu@CNFs reference sample. Fig. 4 **a–d** shows that all samples are able to generate a number of products, including H_2 from H_2O reduction, and CO, CH_4, C_2H_4, ethanol and *n*-propanol etc. from CO_2RR. **Fig. S5** shows the gases produced using different samples. The wide range of CO_2RR products is a characteristic of Cu-based catalysts, indicating that the Cu surface is exposed to the electrolyte and CO_2. With an increase in Ce concentration, the hydrogen evolution reaction (HER) is suppressed, from an average of ~27% for Cu@CNFs to less than 20% for Cu/CeO_x@CNFs-2. The lower H_2 FE is compensated by the increased CO_2RR selectivity, particularly the CO FE. For example, the FE of CO increased from 34.1% for Cu@CNFs to 59.2% for Cu/CeO_x@CNFs-2 at 100 mA cm^{-2}. On the other hand, the CeO_x@CNFs reference catalyst exhibits the highest H_2 FE, reaching about 80%, while the FE of CO is below 1%, which indicates that the CeO_x@CNFs catalyst is not active for CO_2RR. In addition, compared with samples containing Cu–CeO_x, Cu@CNFs shows higher formate FE at low overpotentials and higher hydrocarbon selectivity at higher overpotentials. These results clearly indicate that a combination of Cu and CeO_x is the key to enhanced CO selectivity, with a better performance than either material alone. Recently, many researchers have presented CO_2RR as a promising alternative route for producing syngas (a mixture of CO and H_2) for methanol synthesis (CO/H_2 ratio of 0.5), syngas fermentation (CO/H_2 ratio of 1 to 3.33), and Fischer-Tropsch synthesis (CO/H_2 ratio of 1.67) [24,25]. Here we show that by optimizing the Cu/CeO_x ratio, the CO/H_2 ratios can be tuned in a broad range (from ~ 0 to > 4), demonstrating the high potential of this catalytic system in existing industrial applications.

In addition, due to the use of a flow cell for the electrochemical measurements, we can achieve much higher current densities at much lower potential than other Cu–Ce catalysts tested in a H-cell **(Table S2)**. Specifically, for the Cu/CeO_x@CNFs-2 catalyst, the FE of CO remained above 50% from 50 mA cm^{-2} to 200 mA cm^{-2}, corresponding to −0.50 V (vs. RHE) to −0.65 V (vs. RHE). To the best of our knowledge, this catalyst exhibited higher CO selectivity and current density at the lowest overpotential compared with other Cu–Ce catalysts for CO_2RR (**Table S2**). The electrochemically active surface area (ECSA) was calculated using the double-layer capacitance measured in 0.1 M $KClO_4$ solution (**Fig. S6**). As revealed in Fig. 4**f**, the ESCA of Cu/CeO_x@CNFs-2 (13.22 mF cm^{-2}) is much higher than that of Cu-CNFs (8.35 mF cm^{-2}). The large ECSA of the catalyst is attributed to the special fiber morphology induced by the increasing Ce concentration, from which we can conjecture that more active sites are exposed on the surface where CO_2 can absorb and react.

3.3. Synergistic effect of Cu–CeO_x on CO_2RR

To illustrate the influence of the surface state of the Cu/CeO_x@CNFs catalysts on their catalytic performance, XPS analysis was carried out. Fig. 5**a** shows the Cu 2p XPS spectra of different catalysts. The XPS peak centers at 932.5 eV and 934.6 eV are assigned to the Cu $2p_{3/2}$ peak, and those at 952.5 eV and 953.7 eV may be ascribed to the Cu $2p_{1/2}$ peak [26]. Furthermore, the peak at 932.5 eV corresponds to Cu^0 or Cu^+, and the peak at 934.6 eV is assigned to Cu^{2+}. The results given in **Table S1** and Fig. 5**a** show that a substantial amount of Cu^{2+} appears on the surface of the catalysts, particularly for catalysts with a higher Ce:Cu ratio. This indicates that during the carbonization process, a high ratio of CeO_x stabilizes the oxidized Cu species, avoiding the complete reduction due to the mobility of the oxygen from CeO_x [27]. Meanwhile, the Ce 3d XPS spectra are fitted into eight peaks corresponding to Ce $3d_{5/2}$ (v_0, 882.74 eV; v, 885.28 eV, v′, 889.0 eV; v″, 898.6 eV) and Ce $3d_{3/2}$ (u_0, 901.1 eV; u, 903.7 eV; u′, 907.7 eV; u”, 916.7 eV) [23,28,29]. In particular, v′ and u are assigned to Ce^{3+}, while the others are assigned to Ce^{4+} species. Therefore, Fig. 4**b** indicates a mixture of Ce^{3+} and Ce^{4+} present on the surface of all the catalysts. As the presence of Ce^{3+} requires oxygen vacancies to maintain the electroneutrality of the lattice, we expect that the Cu/CeO_x@CNFs-2 catalyst with the highest Ce^{3+} to Ce^{4+} ratio (**Table S1**) would have the highest density of defects on the surface [23,30].

To further examine the structural defects in the Cu/CeO_x@CNFs catalysts, EPR and Raman spectroscopy were performed (Fig. 6). The EPR signal (g = 2.003), shown in Fig. 6**a**, originates from the unpaired electrons at the oxygen vacancy site [31,32], indicating that defects exist in the sample. **In** Fig. 6**b, a** high intensity peak at ~ 450 cm^{-1} can be observed, corresponding to the F_{2g} vibration mode of CeO_2 [33,34]. Compared with the CeO_x-CNFs, a red shift appeared when the samples contained Cu, indicating that Cu affected the lattice structure of surface CeO_x. The broad peak at ~600 cm^{-1} can be ascribed to the presence of oxygen vacancies [32]. The peak intensities of this band for the Cu/CeO_x@CNFs-n catalysts are higher than for the control sample without Cu (CeO_x@CNFs), demonstrating that Cu can promote the formation of defects. Furthermore, Cu species in the Cu/CeO_x@CNFs-n catalysts can be fully reduced to metallic Cu during CO_2RR, which can then enhance the reduction of Ce^{4+} to Ce^{3+}, leading to an increased ratio of defects [10].

Based on the above results, we conclude that the high CO_2RR activity and CO selectivity can be attributed to the synergetic effects of Cu and CeO_x. We now discuss how the synergetic effects influence the catalytic performance. It is generally accepted that the electroreduction of CO_2 to CO takes place in three steps: (1) adsorption of CO_2; (2) hydrogenation of CO_2 to *COOH; and (3) reduction of *COOH to CO [35]. In the first reaction step, the addition of CeO_x increases the surface area and ECSA of the catalyst, so the adsorption of CO_2 on the catalyst surface is enhanced. In addition, the presence of defects in CeO_x can also facilitate the adsorption of CO_2 on both CeO_x and Cu sites [23,36]. The second reaction step requires a stable adsorption configuration for *COOH to make the reaction pathway thermodynamically favorable. Recently, using density functional theory (DFT), researchers have found that *COOH prefers to adsorb at the interface of two different metal atoms [8,10]. Thus, we suggest that at the Cu–CeO_x interface, the C atom binds to an interfacial Cu site and the O atom binds to the metal

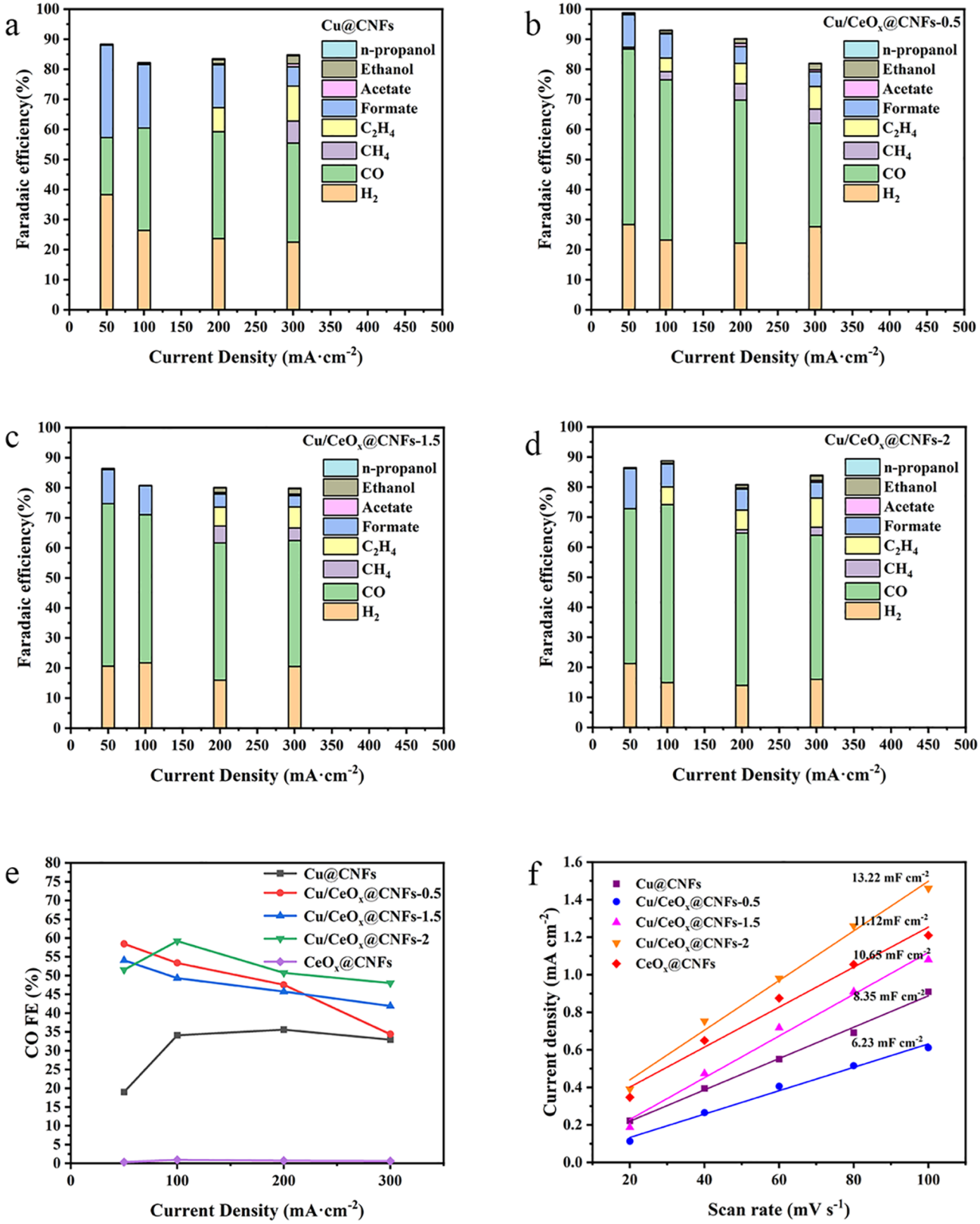

Fig. 4. Faradaic efficiencies of (a) Cu@CNFs, (b) Cu/CeO_x@CNFs-0.5, (c) Cu/CeO_x@CNFs-1.5, and (d) Cu/CeO_x@CNFs-2. (e) FE of CO for various samples. (f) Electric double layer capacitance.

Ce site (which has a greater oxygen affinity) to form a stabilized *COOH adsorption structure. Reduction of *COOH to *CO is usually an energetically downhill step [8,35], and therefore is not significantly affected by the addition of CeO_x. Apart from the CO_2 to CO reaction, CeO_x can also influence the HER and other CO_2RR pathways. For example, at the Cu–CeO_x interface, Cu sites have comparatively weaker binding energies towards *H [10], which explains the lower H_2 selectivity on Cu/CeO_x@CNFs-n catalysts compared with Cu@CNFs. On the other

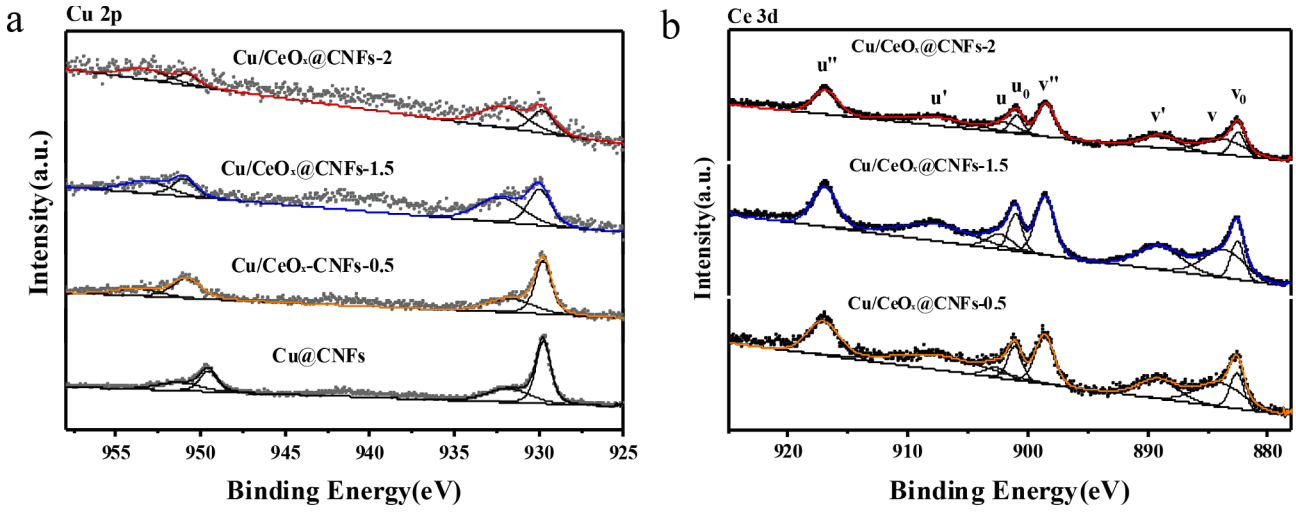

Fig. 5. XPS spectra of (a) Cu 2p and (b) Ce 3d for Cu@CNFs, Cu/CeO_x@CNFs-0.5, Cu/CeO_x@CNFs-1.5, and Cu/CeO_x@CNFs-2.

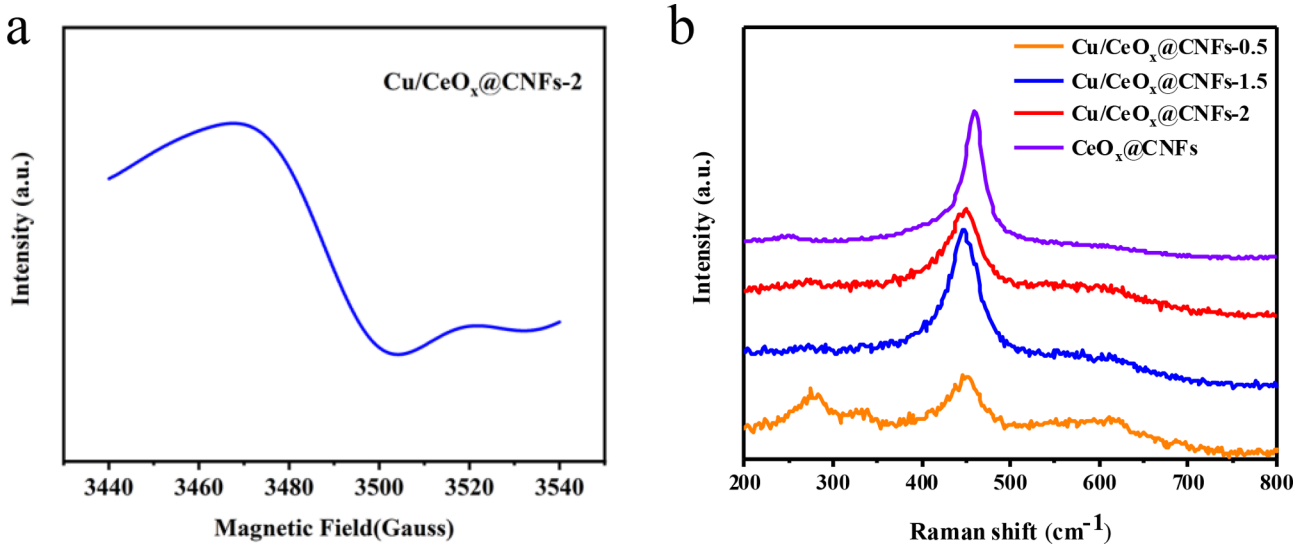

Fig. 6. (a) EPR spectra of Cu/CeO_x@CNFs-2 and (b) Raman spectra of Cu@CNFs, Cu/CeO_x@CNFs-0.5, Cu/CeO_x@CNFs-1.5, and Cu/CeO_x@CNFs-2.

hand, *OCHO may adsorb too strongly at the Cu–CeO_x interface, thus limiting the production of formate. In addition, increased coverage of CeO_x on Cu (Table S1) could block some of the Cu sites, reducing the chance of C–C coupling and leading to decreased C_{2+} product selectivity.

4. Conclusions

In summary, we developed a facile and scalable electrospinning method to synthesize carbon nanofibers decorated with abundant metal–metal oxide interfaces for CO_2RR. Addition of ceria was found to enhance the activity and CO-selectivity as well as decrease the selectivity of HER. With an optimized Cu:Ce ratio, the Cu/CeO_x@CNFs-2 catalyst exhibited a high selectivity towards CO_2RR (up to 85.2%) and CO (up to 59.2%) at −0.6 V (vs. RHE), with a high current density of 100 mA cm^{-2}. The improved catalytic performance has been attributed to the high surface area of the catalyst and the synergy between Cu and CeO_x, including improved CO_2 adsorption ability and optimized adsorption strength towards different reaction intermediates. This work suggests an approach for the future design and application of metal–-oxide-based catalysts for the electroreduction of CO_2.

CRediT authorship contribution statement

Xin Zong: Conceptualization, Resources, Writing - original draft. **Jie Zhang:** Validation. **Jinqiu Zhang:** Writing - review & editing, Supervision. **Wen Luo:** Writing - review & editing, Supervision. **Andreas Züttel:** Funding acquisition. **Yueping Xiong:** Supervision, Project administration, Funding acquisition.

Declaration of Competing Interest

The authors declare that they have no known competing financial interests or personal relationships that could have appeared to influence the work reported in this paper.

Acknowledgements

This research is supported by the Swiss National Science Foundation (No. PZ00P2_179989), Switzerland. This research is also part of the activities of SCCER HeE, which is financially supported by Innosuisse-Swiss Innovation Agency, Switzerland. The authors thank beamline BL14B1 (Shanghai Synchrotron Radiation Facility) for providing the beam time and for help during the experiments.

Appendix A. Supplementary data

Supplementary data to this article can be found online at https://doi.org/10.1016/j.elecom.2020.106716.

References

[1] M. Willeit, A. Ganopolski, R. Calov, V. Brovkin, Mid-Pleistocene transition in glacial cycles explained by declining CO_2 and regolith removal, Sci. Adv. 5 (2019) evva7337.

[2] D.T. Whipple, P.J.A. Kenis, Prospects of CO_2 utilization via direct heterogeneous electrochemical reduction, J. Phys. Chem. Lett. 1 (2010) 3451–3458.

[3] K. Nakata, T. Ozaki, C. Terashima, A. Fujishima, Y. Einaga, High-yield electrochemical production of formaldehyde from CO_2 and seawater, Angew Chem. Int. Ed. Engl. 53 (2014) 871–874.

[4] E.E. Benson, C.P. Kubiak, A.J. Sathrum, J.M. Smieja, Electrocatalytic and homogeneous approaches to conversion of CO_2 to liquid fuels, Chem. Soc. Rev. 38 (2009) 89–99.

[5] L.B. Wang, W.B. Zhang, X.S. Zheng, Y.Z. Chen, W.L. Wu, J.X. Qiu, X.C. Zhao, X. Zhao, Y.Z. Dai, J. Zeng, Incorporating nitrogen atoms into cobalt nanosheets as a strategy to boost catalytic activity toward CO_2 hydrogenation, Nat. Energy 2 (2017) 868–876.

[6] D. Kim, C.L. Xie, N. Becknell, Y. Yu, M. Karamad, K. Chan, E.J. Crumlin, J.K. Norskov, P.D. Yang, Electrochemical activation of CO_2 through atomic ordering transformations of AuCu nanoparticles, J. Am. Chem. Soc. 139 (2017) 8329–8336.

[7] Y. Hori, A. Murata, S. Ito, Enhanced evolution of Co and suppressed formation of hydrocarbons in electroreduction of Co_2 at a copper electrode modified with cadmium, Chem. Lett. (1990) 1231–1234.

[8] W. Luo, W. Xie, R. Mutschler, E. Oveisi, G.L. De Gregorio, R. Buonsanti, A. Züttel, Selective and stable electroreduction of CO_2 to CO at the copper/indium interface, ACS Catal. 8 (2018) 6571–6581.

[9] D. Raciti, K.J. Livi, C. Wang, Correction to Highly dense Cu nanowires for low-overpotential CO_2 reduction (vol 15, pg 6829, Nano Lett. 16 (2016) (2015) 6716-6716.

[10] S.B. Varandili, J. Huang, E. Oveisi, G.L. De Gregorio, M. Mensi, M. Strach, J. Vavra, C. Gadiyar, A. Bhowmik, R. Buonsanti, Synthesis of Cu/CeO_{2-x} nanocrystalline heterodimers with interfacial active sites to promote CO_2 electroreduction, ACS Catal. 9 (2019) 5035–5046.

[11] H.P. Yang, Y. Wu, G.D. Li, Q. Lin, Q. Hu, Q.L. Zhang, J.H. Liu, C. He, Scalable production of efficient single-atom copper decorated carbon membranes for CO_2 electroreduction to methanol, J. Am. Chem. Soc. 141 (2019) 12717–12723.

[12] P. De Luna, R. Quintero-Bermudez, C.-T. Dinh, M.B. Ross, O.S. Bushuyev, P. Todorović, T. Regier, S.O. Kelley, P.D. Yang, E.H. Sargent, Catalyst electro-redeposition controls morphology and oxidation state for selective carbon dioxide reduction, Nat. Catal. 1 (2018) 103–110.

[13] J. Gurudayal, D.F. Bullock, C.M. Srankó, Y.W. Towle, M. Lum, M.C. Hettick, A. Scott, J. Javey, Ager, Efficient solar-driven electrochemical CO_2 reduction to hydrocarbons and oxygenates, Energy Environ. Sci. 10 (2017) 2222–2230.

[14] K. Jiang, R.B. Sandberg, A.J. Akey, X.Y. Liu, D.C. Bell, J.K. Norskov, K.R. Chan, H.T. Wang, Metal ion cycling of Cu foil for selective C-C coupling in electrochemical CO_2 reduction, Nat. Catal. 1 (2018) 111–119.

[15] Q. Lu, J. Rosen, F. Jiao, Nanostructured metallic electrocatalysts for carbon dioxide reduction, Chemcatchem. 7 (2015) 38–47.

[16] Z.L. Wang, C.L. Li, Y. Yamauchi, Nanostructured nonprecious metal catalysts for electrochemical reduction of carbon dioxide, Nano Today 11 (2016) 373–391.

[17] H.J. Freund, M.W. Roberts, Surface chemistry of carbon dioxide, Surf. Sci. Rep. 25 (1996) 225–273.

[18] D.F. Gao, Y. Zhang, Z.W. Zhou, F. Cai, X.F. Zhao, W.G. Huang, Y.S. Li, J.F. Zhu, P. Liu, F. Yang, G.X. Wang, X.H. Bao, Enhancing CO_2 electroreduction with the metal–oxide interface, J. Am. Chem. Soc. 139 (2017) 5652–5655.

[19] J.-H. Kim, H. Woo, J. Choi, H.-W. Jung, Y.-T. Kim, CO_2 electroreduction on Au/TiC: enhanced activity due to metal–support interaction, ACS Catal. 7 (2017) 2101–2106.

[20] T.Y. Yang, W. Wen, G.Z. Yin, X.L. Li, M. Gao, Y.L. Gu, L. Li, Y. Liu, H. Lin, X.M. Zhang, B. Zhao, T.K. Liu, Y.G. Yang, Z. Li, X.T. Zhou, X.Y. Gao, Introduction of the X-ray diffraction beamline of SSRF, Nucl. Sci. Tech. 26 (2015) 020101.

[21] J. Zhang, W. Luo, A. Züttel, Self-supported copper-based gas diffusion electrodes for CO_2 electrochemical reduction, J. Mater. Chem. A (2019) 26285–26292.

[22] Z. Wang, S.J. Peng, Y.X. Hu, L.L. Li, T. Yan, G.R. Yang, D.X. Ji, M. Srinivasan, Z.J. Pan, S. Ramakrishna, Cobalt nanoparticles encapsulated in carbon nanotube-grafted nitrogen and sulfur co-doped multichannel carbon fibers as efficient bi-functional oxygen electrocatalysts, J. Mater. Chem. A 5 (2017) 4949–4961.

[23] Y. Wang, Z. Chen, P. Han, Y. Du, Z. Gu, X. Xu, G. Zheng, Single-atomic Cu with multiple oxygen vacancies on ceria for electrocatalytic CO_2 reduction to CH_4, ACS Catal. 8 (2018) 7113–7119.

[24] B. Qin, Y. Li, H. Fu, H. Wang, S. Chen, Z. Liu, F. Peng, Electrochemical reduction of CO_2 into tunable syngas production by regulating the crystal facets of earth-abundant Zn catalyst, ACS Appl. Mater. Interf. 10 (2018) 20530–20539.

[25] W. Sheng, S. Kattel, S. Yao, B. Yan, Z. Liang, C.J. Hawxhurst, Q. Wu, J.G. Chen, Electrochemical reduction of CO_2 to synthesis gas with controlled CO/H_2 ratios, Energy Environ. Sci. 10 (2017) 1180–1185.

[26] W.-W. Wang, W.-Z. Yu, P.-P. Du, H. Xu, Z. Jin, R. Si, C. Ma, S. Shi, C.-J. Jia, C.-H. Yan, Crystal plane effect of ceria on supported copper oxide cluster catalyst for CO oxidation: importance of metal–support interaction, ACS Catal. 7 (2017) 1313–1329.

[27] W.-W. Wang, P.-P. Du, S.-H. Zou, H.-Y. He, R.-X. Wang, Z. Jin, S. Shi, Y.-Y. Huang, R. Si, Q.-S. Song, C.-J. Jia, C.-H. Yan, Highly dispersed copper oxide clusters as active species in copper-ceria catalyst for preferential oxidation of carbon monoxide, ACS Catal. 5 (2015) 2088–2099.

[28] J. Han, J. Meeprasert, P. Maitarad, S. Nammuangruk, L. Shi, D. Zhang, Investigation of the facet-dependent catalytic performance of Fe_2O_3/CeO_2 for the selective catalytic reduction of NO with NH_3, J. Phys. Chem.C 120 (2016) 1523–1533.

[29] R.H. Gao, D.S. Zhang, P. Maitarad, L.Y. Shi, T. Rungrotmongkol, H.R. Li, J.P. Zhang, W.G. Cao, Morphology-dependent properties of MnO_x/ZrO_2 CeO_2 nanostructures for the selective catalytic reduction of NO with NH_3, J. Phys. Chem. C 117 (2013) 10502–10511.

[30] Z. Hu, X.F. Liu, D.M. Meng, Y. Guo, Y.L. Guo, G.Z. Lu, Effect of ceria crystal plane on the physicochemical and catalytic properties of Pd/ceria for CO and propane oxidation, ACS Catal. 6 (2016) 2265–2279.

[31] N. Zhang, X.Y. Li, H.C. Ye, S.M. Chen, H.X. Ju, D.B. Liu, Y. Lin, W. Ye, C.M. Wang, Q. Xu, J.F. Zhu, L. Song, J. Jiang, Y.J. Xiong, Oxide defect engineering enables to couple solar energy into oxygen activation, J. Am. Chem. Soc. 138 (2016) 8928–8935.

[32] Z. Xiao, Y. Li, F. Hou, C. Wu, L. Pan, J. Zou, L. Wang, X. Zhang, G. Liu, G. Li, Engineering oxygen vacancies and nickel dispersion on CeO_2 by Pr doping for highly stable ethanol steam reforming, Applied Catalysis B: Environmental 258 (2019) 117940.

[33] D. Harshini, D.H. Lee, J. Jeong, Y. Kim, S.W. Nam, H.C. Ham, J.H. Han, T.H. Lim, C.W. Yoon, Enhanced oxygen storage capacity of $Ce_{0.65}Hf_{0.25}M_{0.1}O_2$-delta (M = rare earth elements): Applications to methane steam reforming with high coking resistance, Appl. Catal. B Environ. 148 (2014) 415–423.

[34] D.K. Chen, D.D. He, J.C. Lu, L.P. Zhong, F. Liu, J.P. Liu, J. Yu, G.P. Wan, S.F. He, Y.M. Luo, Investigation of the role of surface lattice oxygen and bulk lattice oxygen migration of cerium-based oxygen carriers: XPS and designed H-2-TPR characterization, Appl. Catal. B Environ. 218 (2017) 249–259.

[35] A.A. Peterson, F. Abild-Pedersen, F. Studt, J. Rossmeisl, J.K. Nørskov, How copper catalyzes the electroreduction of carbon dioxide into hydrocarbon fuels, Energy Environ. Sci. 3 (2010) 1311–1315.

[36] P.M. Albrecht, D.-E. Jiang, D.R. Mullins, CO_2 adsorption as a flat-lying, tridentate carbonate on CeO_2(100), J. Phys. Chem. C 118 (2014) 9042–9050.